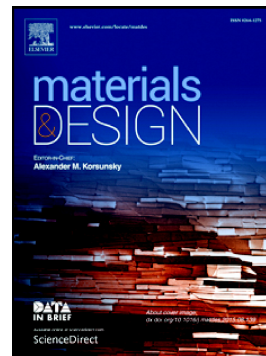


Accepted Manuscript

On the measurement of relative powder-bed compaction density in powder-bed additive manufacturing processes

Usman Ali, Yahya Mahmoodkhani, Shahriar Imani Shahabad, Reza Esmaeilizadeh, Farzad Liravi, Esmat Sheydaeian, Ke Yin Huang, Ehsan Marzbanrad, Mihaela Vlasea, Ehsan Toyserkani



PII: S0264-1275(18)30497-0
DOI: doi:[10.1016/j.matdes.2018.06.030](https://doi.org/10.1016/j.matdes.2018.06.030)
Reference: JMADE 4000
To appear in: *Materials & Design*
Received date: 5 April 2018
Revised date: 28 May 2018
Accepted date: 15 June 2018

Please cite this article as: Usman Ali, Yahya Mahmoodkhani, Shahriar Imani Shahabad, Reza Esmaeilizadeh, Farzad Liravi, Esmat Sheydaeian, Ke Yin Huang, Ehsan Marzbanrad, Mihaela Vlasea, Ehsan Toyserkani , On the measurement of relative powder-bed compaction density in powder-bed additive manufacturing processes. *Jmade* (2018), doi:[10.1016/j.matdes.2018.06.030](https://doi.org/10.1016/j.matdes.2018.06.030)

This is a PDF file of an unedited manuscript that has been accepted for publication. As a service to our customers we are providing this early version of the manuscript. The manuscript will undergo copyediting, typesetting, and review of the resulting proof before it is published in its final form. Please note that during the production process errors may be discovered which could affect the content, and all legal disclaimers that apply to the journal pertain.

Revised**On the measurement of relative powder-bed compaction density in powder-bed additive manufacturing processes**

Usman Ali, Yahya Mahmoodkhani, Shahriar Imani Shahabad, Reza Esmailizadeh, Farzad Liravi, Esmat Sheydaeian, Ke Yin Huang, Ehsan Marzbanrad, Mihaela Vlasea, Ehsan Toyserkani

Multi-Scale Additive Manufacturing Lab, University of Waterloo, 200 University Avenue West, Waterloo, ON, N2L 3G1, Canada

Re-Submission Date: May 28, 2018

Number of Pages: 15

Number of Figures: 9

Number of Tables: 3

Contact Author: Ehsan Toyserkani, PhD, P.Eng

Address: Department of Mechanical and Mechatronics Engineering, University of Waterloo, Waterloo, Ontario, Canada, N2L 3G1, e-mail: ehsan.toyserkani@uwaterloo.ca

On the measurement of relative powder-bed compaction density in powder-bed additive manufacturing processes

Abstract

Experimental studies in the literature have identified the powder-bed compaction density as an important parameter, governing the quality of additively manufactured parts. For example, in laser powder-bed fusion (LPBF), the powder-bed compaction density directly affects the effective powder thermal conductivity and consequently the temperature distribution in melt pool. In this study, this physical parameter in a LPBF build compartment is measured using a new methodology. A UV curable polymer is used to bind powder-bed particles at various locations on the powder-bed compartment when Hastelloy X was used. The samples are then scanned using a nano-computing tomography (CT) system at high resolution to obtain an estimation of the relative powder-bed compaction density. It is concluded that due to the interaction between the recoater and the variation in the powder volume accumulated ahead of the recoater across the build compartment, the relative powder-bed compaction density decreases along the recoater moving direction (from 66.4% to 52.4%). This variation in the powder-bed compaction density affects the density and surface roughness of the final printed parts that is also investigated. Results show that the part density and surface quality decrease ~0.25% and ~20%, respectively, along the build bed in direction of the recoater motion.

Keywords: Additive manufacturing, 3D printing, compaction density, selective laser melting, laser powder-bed fusion, Hastelloy X

1 Introduction

Additive manufacturing (AM) has gained a new momentum in many industrial sectors [1], [2]. AM processes are becoming more common in the product development lifecycle because of their remarkable capabilities of manufacturing complex geometries compared to conventional manufacturing methods. For instance, manufacturing of complex shapes and consolidation of assemblies are now feasible without the use of multiple manufacturing steps, thus saving time and resources [3]. One of the disadvantages of AM techniques, however, is the cost of raw materials and low repeatability [4].

There are various powder-bed AM processes that are classified based on the powder joining mechanisms. The most common methods of joining powder particles in powder-bed systems are the deployment of thermal energy generated by the irradiation of laser, electron beam, and plasma, or the use of binders [5]–[7]. In the binder jetting 3D printing process, powder particles are adhered to each other using a liquid-based binder that is jetted through a printhead at selected locations within each layer [5]. Electron beam and laser processes adhere the powder particles by melting or sintering. Laser powder-bed based AM processes are commonly known as Laser Beam Melting (LBM), Selective Laser Melting (SLM), Laser Powder-bed Fusion (LPBF) [2].

Laser powder-bed fusion (LPBF) is categorized as one of the main metal AM processes based on ASTM standard ISO/ASTM 52900 [8]. The LPBF process consists of a series of steps for manufacturing complex parts by typically using a high intensity laser as an energy source to melt and fuse selective regions of powder, layer-by-layer, to build the final shape [9]. Similar to other AM processes, LPBF includes various process parameters. The most common process parameters studied in the literature include laser power, scanning speed, hatch spacing, layer thickness etc. [10], [11] that need to be optimized for achieving high quality parts [12]. In addition to the above mentioned laser process parameters, one of such parameters, which can significantly affect the final product properties (e.g., density, surface roughness) is the powder-bed compaction density in the build compartment [13], [14]. In general, the successful industry adoption of metal AM relies on understanding the complex interactions between the design, the used materials, and the process to ensure high product quality and reliability. These relationships are typically developed using costly empirical approaches. To enable a lean manufacturing approach, simulations, monitoring and process control of LPBF are becoming a high interest research and development area [15].

In order to effectively simulate the complex laser-material interaction occurring during the LPBF process, the relative values for powder compaction density in the powder-bed are required [16]–[18]. For example, Denlinger et al. [19] used volume of voids between particles as input to their simulations to calculate thermal history. Other researchers used various types of functions to relate the bulk and powder densities of materials [16], [17]. Powder-scale simulations, such as Discrete Element Method (DEM), do not consider the powder-bed compaction density as they can directly account for the powder distribution and packing in the powder-bed [20]. Due to the lack of information in the literature on the exact values for the powder-bed compaction density, this process property is assumed a fixed number across the bed, where in many cases the chosen values are approximated [16], [18]. Therefore, it is important to develop a systematic approach for the measurement of powder-bed compaction density as this parameter directly governs the final part quality and the simulated behavior of the laser-material interaction [21].

There are various methods presented in the literature to quantify the powder-bed compaction density during AM processes. Liu et al. [14] investigated the effect of powder-bed compaction density on the final part properties by printing a 30 x 30 x 30 mm container during the AM process and weighing the powder inside. They concluded that a wider range of particle size distribution provides higher powder-bed compaction density and results in parts with high density and surface quality. Jacob et al. [13] conducted an experimental study to measure the powder-bed density. They used a custom container (closed hollow

cylinder with a conical lid), which captured the loose powder inside the container during the process from various locations on the build plate. Karapatis et al. [22] studied the powder-bed compaction density across the build compartment using a similar technique and have also discussed ‘wall effects’ on the powder-bed density due to the presence of container. Similarly, Elliott et al. [5] studied the effect of powder particle size and distribution on powder-bed compaction density during binder-jet AM. They suggested that the particle size distribution with a median particle size (D_{50}) closer to $25\ \mu\text{m}$ is an ideal size for high powder-bed density. However, they did not investigate the reason or effect of differences in powder-bed densities on AM-made parts. Most of the powder-bed density measuring techniques discussed involve using containers/vessels and are therefore process dependant. Due to the interaction between the powder recoating mechanism and the build bed during the manufacturing process, the powder density may be significantly affected by the design of the powder capture artefacts. In addition, the evaluation of the internal volume of these powder capture vessels and the volume of captive particles in them results in a high level of uncertainty in estimating the powder-bed density.

The discussion presented shows the direct correlation between powder-bed compaction density and the particle size distribution. In addition, various studies show the effect of powder distribution on the final part quality [6]. Experimental work by McGeary [23] illustrates the effect of powder size distribution on the powder-bed densities. Spierings et al. [24] have used 316L stainless steel powders with D_{50} of $15\ \mu\text{m}$ and $28\ \mu\text{m}$ to produce parts with higher density than steel powders with D_{50} of $38\ \mu\text{m}$. There have been many studies on the effect of particle size distribution on the sintering process of metals and ceramics (e.g. [25], [26]).

The literature lacks comprehensive studies on accurate measurement of powder-bed compaction density and its cause and effect on AM-made parts. To the best knowledge of authors, there are no studies in the literature, which focus on process-independent methods to measure the powder-bed compaction density. The aim of this paper is twofold. Firstly, a new method to measure the relative powder-bed compaction density is proposed by encapsulating particle samples through highly precise injection of a UV- curable low-viscous polymer at select locations in the build bed, followed by density measurement of the samples using 3D nano-CT. Secondly, the effect of relative compaction density on the final part quality is investigated. In this regard, density and surface roughness are measured in the AM-made parts printed on different locations of the build bed. Results show differences in the density and roughness of AM-made parts thus highlighting the importance of powder-bed compaction density.

2 Experimental procedures

2.1 Powder material characterization

Commercially available Hastelloy X powder from EOS GmbH (EOS NickelAlloy HX, Krailling, Germany) with a D10 (diameter at 10% cumulative volume), D50 (median diameter) and D90 (diameter at 90% cumulative volume) of 15 μm , 30 μm and 46 μm respectively was used in this study. An average material composition for each element of Hastelloy X alloy provided by EOS® is given in Table 1.

Table 1: Elemental composition of Hastelloy X

Element	Cr	Fe	Mo	W	Co	C	Si	Mn	S	P	B	Cu	Al	Ti	Ni
Weight %	21	18	9	0.7	1.5	0.1	1	1	0.03	0.04	0.01	0.5	0.50	0.15	Bal.

An EOS M290 (EOS GmbH, Krailling, Germany) was used for the LPBF process and relative powder-bed compaction density measurements. Parts were printed with laser power of 220 W and speed of 1000 mm/s with a layer thickness of 60 μm . All other parameters such as scanning strategies, core and skin parameters, etc. were kept as default for all parts

A dynamic optical particle analyzer (Retsch Camsizer X2, Retsch Technology GmbH, Haan, Germany) was used to measure the powder size distribution from various locations on the build bed. Surface roughness measurements of metal LPBF samples were taken with a high performance confocal laser scanning microscope (Keyence VK-X250, Keyence Corporation, Osaka, Japan). Density measurements of the LPBF samples (ρ_p) were taken using a temperature corrected Archimedes water displacement method using the equation:

$$\rho_p = \frac{W_D \rho_w}{W_D - W_W} \quad \text{Eq. 1}$$

where W_D is the dry weight, W_W is the wet weight and ρ_w is the temperature corrected density of distilled water ASTM B311-17 [27].

2.2 Relative compaction density measurement technique

In this work, an ultraviolet (UV) curable polymer was used to measure the relative powder-bed compaction density. The UV curable polymer was made using 95% Bisphenol-A ethoxylated diacrylate (BAE) and 5% of a photoinitiator powder (5 wt%), phosphine oxide (Irgacure 819) [28]. It is important to mention that one of the advantages of using a polymer to bind the powder over the powder capture artefact or powder sampling techniques is that the powders are not disturbed by the sampling technique, nor by the powder recoating mechanism interacting with the walls of the powder capture vessel or artefact. However, the disadvantage of using a polymer is the droplet impact kinetics and the liquid spreading mechanisms [29], [30]. The impact kinetics can be minimized by having the polymer dispensing nozzle as close as possible to the powder build bed, whereas the liquid spreading mechanisms are influenced by the flowability and viscosity of the dispensed polymer. The flowability of any fluid is a function of different parameters such as media pore size and distribution, liquid-solid interfacial parameters (surface tension, contact angle) and the viscosity of the liquid [28], [31]. If the polymer has low viscosity and flowability, the primary and secondary liquid spread mechanisms occur fast, while the polymer covering a large area on the powder-bed without being able to join the powder layers effectively (Figure 4a). On the other hand, if the polymer is highly viscous, the sessile polymer droplet attaches to the powder-bed and disturbs the top layer of powder during the primary liquid spread phase; in the secondary phase of liquid imbibition, the powders may be dislodged, with it causing a dip in the powder-bed, substantially changing the compaction density (Figure

4b). Therefore, it is necessary to use proper polymer composition to achieve effective powder-bed compaction density samples. The composition of the polymer used in this paper has been selected based on empirical observations, where no dip was observed in the powder after infiltration, and the samples had proper integrity during handling after UV curing (Figure 4c).

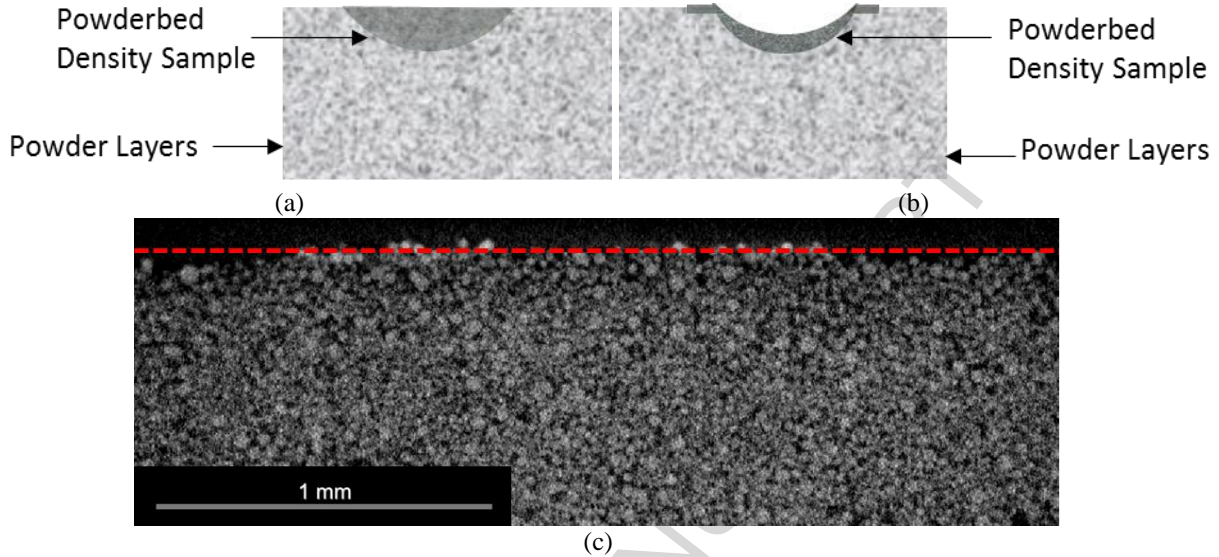


Figure 1: Schematic showing the potential effect of polymer viscosity on the powder-bed compaction density samples with (a) Less Viscous Polymer (b) High Viscous Polymer (c) A Nano-CT image of the powder-bed compaction density samples showing proper integrity of the samples after UV curing

The UV curable polymer was dispensed onto Hastelloy X powder material in the build compartment of EOS M290 at selected locations in the Front (F), Middle (M) and Back (B) of the build bed (Figure 3). The powder-bed in the build bed was prepared by laying down 100 powder layers of 20 μm layer thickness relative to the base plate substrate in the build bed. UV curable polymer was dispensed on the powder-bed using a Nordson EFD (Nordson EFD, RI, USA) pneumatic liquid dispensing system with an Ultimius V controller system (Nordson EFD RI, USA) from a height of 5 mm (Figure 2a). As discussed previously, the dispensing height was selected to reduce the droplet kinetic effects. A 0.016" diameter needle with a dispensing time of 3 s was used for dispensing UV curable polymer for each sample. Resulting powder-bed compaction density samples were cured (Figure 2b) using an OmniCure S2000 (Excelitas Technologies, ON, Canada) UV curing system with an intensity of 5.4 W/cm^2 for 20 s and left overnight. Figure 2a shows the dispensing system on the powder-bed, and Figure 2b shows the samples being cured. The dotted circles show samples in the Front (F) and Middle (M) of the powder-bed.

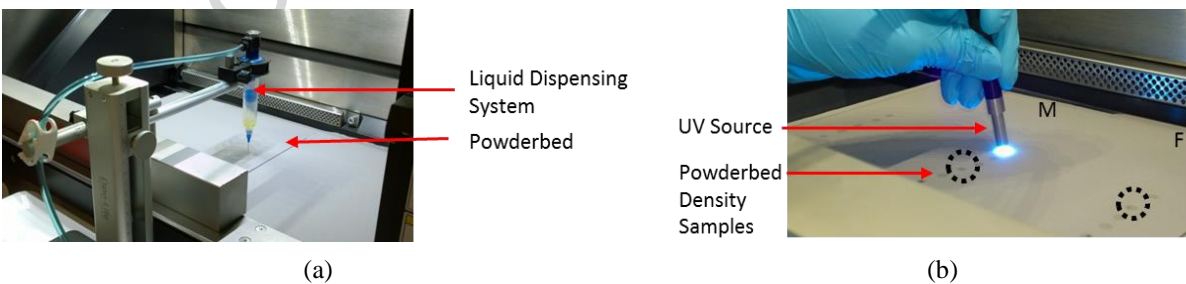


Figure 2: (a) UV curable polymer dispensing system (b) Curing powder-bed compaction density samples

To achieve a statistically representative sample set, 5 samples were prepared at the Front (F), Middle (M) and Back (B) of the powder-bed (Figure 3). In Figure 3, F represents the samples nearest to the recoater

initial position along the spread path, while M and B refer to the intermediate and final recoater positions along the spread path.

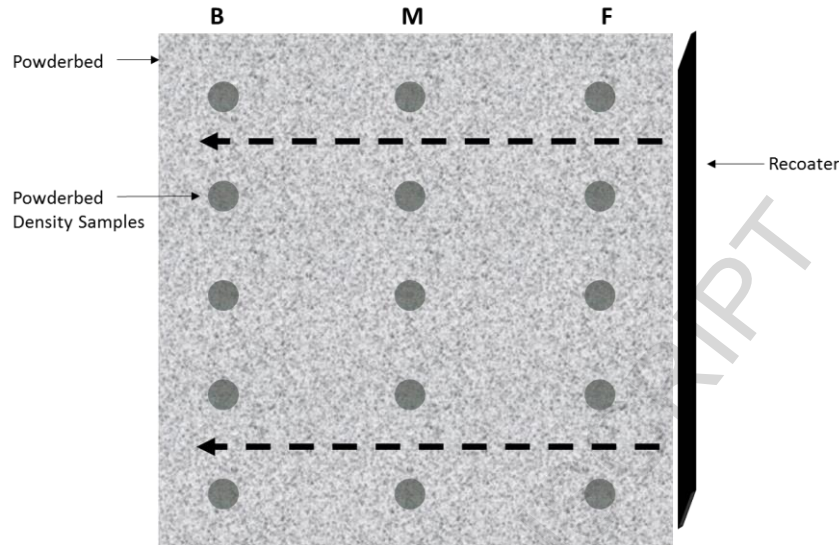


Figure 3: Relative powder-bed compaction density samples configuration on the Front (F), Middle (M) and Back (B) of the powder-bed. The recoater motion is shown with dotted arrows.

The resulting polymer-encapsulated powder samples (Figure 4a) were removed from the powder-bed and CT scanned (Xradia 520 Versa, Zeiss) to measure the powder-bed density using a 4X detector on the UV cured powder-bed density samples with a voxel size of $3\ \mu\text{m}$ at 160 kV, 10W and beam hardening of 0.05 with an exposure time of 4 s for each projection. The greyscale threshold was determined to enable the attenuation of the polymer, thus showcasing the metal particles only in the final CT dataset.

The scanned 3D projections were reconstructed and analyzed using Dragonfly 3.1 to find the solid fraction and thus the approximate powder-bed compaction density for all 15 samples, with one such example illustrated in Figure 4b. Figure 4b shows one such sample, where colors show the different powder particles trapped in the UV cured polymer.

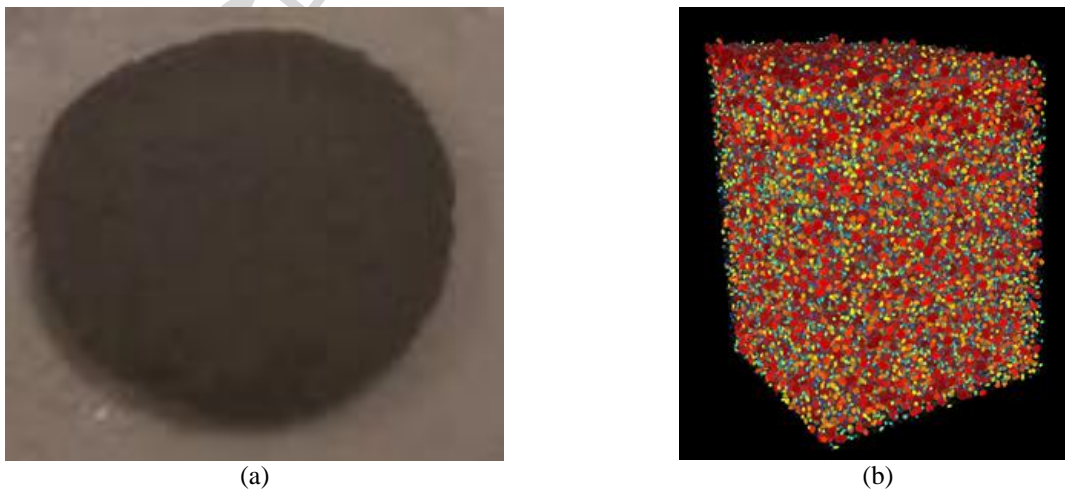


Figure 4: (a) UV cured powder-bed sample (b) Processed Nano-CT 3D image of the metal particles entrapped in the UV polymer sample

The current work focuses on calculating the relative powder-bed compaction densities across the build bed in a LPBF system. The method outlined in this work can be applied to any powder-bed processes such as binder-jet AM.

2.3 Statistical methodology

In this work, relative powder-bed compaction density at 5 locations in the Front, Middle and Back of the build bed were measured. These replicates allow an appropriate statistical study of the effect of build bed locations on powder-bed compaction density. A single factor (powder-bed location) analysis of variance (ANOVA) with a significance level (α) of 0.05 is performed using MATLAB® on the measured powder-bed compaction densities to study if the location on the build bed has an effect ($p - value < \alpha$) on the powder-bed compaction densities.

3 Results and discussion

3.1 Relative powder-bed compaction density in the build compartment

The importance of knowing the powder-bed compaction density in AM processes, and specifically in AM simulations of laser-powder interactions, has been previously highlighted [13], [14], [22]. In this work, the relative powder-bed compaction densities at select locations across the build bed are measured by encapsulating powder using a UV curable polymer resin. Results from Section 2.2 show the methodology used to manufacture and measure the powder-bed compaction density parts using nano-CT. Nano-CT datasets were processed to extract the encapsulated metal powder matrix and completely attenuate the polymer volume fraction, having it appear as a void. Correspondingly, for each of the 15 polymer-encapsulated metal powder samples, the relative powder-bed compaction density was determined using:

$$\rho_{PB} = \frac{V_p}{V_p + V_r} \times 100 \quad \text{Eq. 2}$$

where ρ_{PB} is the relative powder-bed compaction density, V_p is the volume of the particles and V_r is the remaining volume occupied by the polymer and any trapped voids in the encapsulated polymer/metal matrix.

The authors acknowledge the uncertainty margin introduced by using polymer infiltration as a method of capturing powder-bed density. Although no visible deviation is seen in the powder clusters, there are factors that may cause unseen deviation drifting the results from sample to sample. The most important factors contributing to measurement uncertainty are related to the powder-polymer interactions such as, but not limited to, the droplet impact kinetics with the powder-bed, powder migration due to the initial phase in sessile droplet imbibition, as well as the shrinkage due to UV polymer cross-linking. Quantifying the measurement uncertainty for these types of effects is of importance and will be the focus of the authors' upcoming work. In the context of this work, the authors use the measurements to quantify the "relative" change between locations across the build bed and not as "absolute" density measurement values.

Corresponding compaction densities from F, M and B of the powder-bed are shown in Table 2 and Figure 5. Results from Table 2 show the highest powder-bed compaction density (66.4%) near the front of the powder-bed with decreasing densities of 55.8% and 52.4% in the middle and back of the powder-bed, respectively. The respective standard deviation (St Dev) and minimum (Min) and maximum (Max) values for F, M and B of the powder-bed are also shown in Table 2. Results from ANOVA analysis shows a p -value of 0.0052 which proves that the location of the build bed effects the relative powder-bed compaction density.

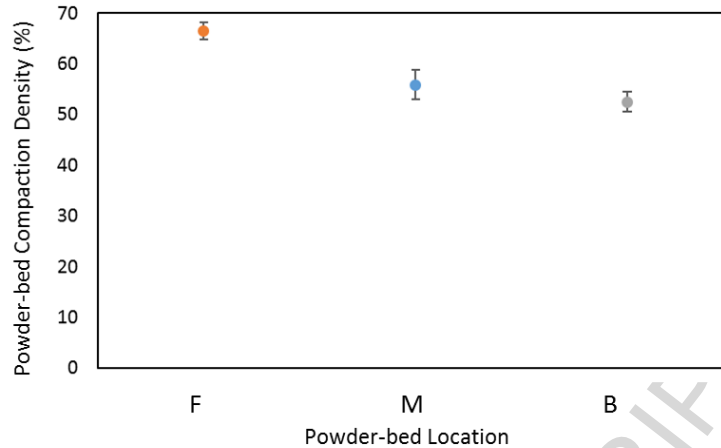


Figure 5: Powder-bed compaction density data from the Front (F), Middle (M) and Back (B) of the build bed

Table 2: Powder-bed compaction density in the Front (F), Middle (M) and Back (B) of the build bed

	Mean (%)	St Dev (%)	Min (%)	Max (%)
F	66.4	3.74	60.5	70.8
M	55.8	6.44	45.5	62.2
B	52.4	4.44	45.8	58.2

It is important to note that the compaction densities decrease along the direction of the recoater movement. This suggests that there is a notable interaction between the recoater blade and the remaining powder front ahead of the recoater, resulting in variable compaction densities across the powder-bed. It is important to characterize this powder-bed density difference and justify an appropriate reasoning behind such differences in the relative powder-bed compaction densities to facilitate effective production of LPBF and other powder-bed system parts. In addition, as mentioned earlier, this would provide helpful data to numerical and analytical models in effectively predicting the powder and part characteristics during LPBF and other powder-bed systems as it effects the powder thermal conductivity [16], [17] and hence the temperature, width and depth of the melt pool [18]–[20].

The authors believe that this difference in powder-bed compaction densities is caused by the effect of recoater used in powder-bed systems. This effect can be attributed to a segregation of particles based on particle size along the powder spread direction of a rigid recoater [32], [33], where smaller particles are depleted first, thus changing the power distribution across the powder-bed and resulting in a decreased powder density along the spread or powder coating direction. The change in powder size distribution and powder-bed density has a direct effect on the laser-material interaction, resulting in variability in terms of product quality in the direction of powder recoating [33], [34].

This hypothesis is illustrated by a schematic in Figure 6. Figure 6a shows a schematic of the LPBF system, where the current layer of powder rests on a solid substrate in the build bed. New powder from the feeding bed is used to supply the next powder layer by using a recoater. In the schematic presented in Figure 6a, letters A, B, C, D mark different areas in the LPBF build chamber, as the recoater moves from the front to the back of the build bed. Figure 6b is an illustration of the change in volume fraction of large and small powder particles as their distribution changes in the powder-bed across the recoating direction. Area A refers to the new powder that is brought from the feeding bed. Similarly, Areas B, C and D refer to the Front, Back and Powder Overflow areas, respectively. It is noted that Areas B and C lie on the build bed,

whereas Area D is the extra powder spilled over after the recoater covers the whole build bed layer. In the current hypothesis, due to powder size segregation along the spread direction, the powder-bed compaction densities are expected to change across the powder-bed. As an illustration, in Figure 6b, new powder contains 7 large and 9 small particles. As the recoater moves from the Front to the Back of the build bed, areas near the Front of the build bed (Figure 6b – Area B) contain higher volume fraction of smaller particles which decreases across the recoater direction (Figure 6b – Area C) while the volume fraction of larger particles increases across the recoater moving direction. These effects are due to factors including the change in the particle size distribution, powder cohesion, Coulomb and rolling friction, van der Waals forces, as well as gravitational effects, as the recoater moves from the front to the back of the build bed.

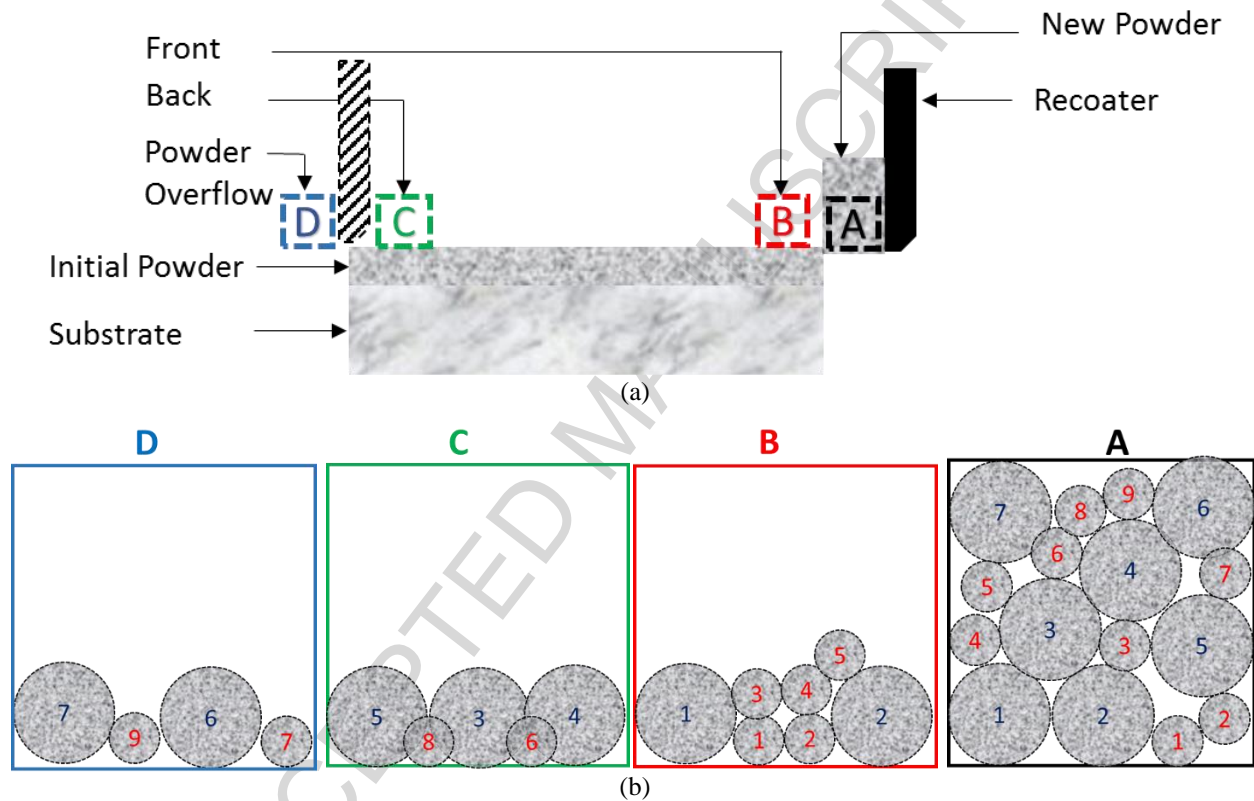


Figure 6: (a) Schematic of LPBF powder-bed system with recoater (b) Schematic to explain the differences in powder-bed compaction density due to powder size effect caused by the recoater

To experimentally validate powder segregation and depletion of small particles along the recoating direction, the particle size near F, M, and B of the build bed should provide a clear indication on the reasons for this difference. To characterize this difference, 3 powder samples from the F, M, and B (Figure 3) of the build bed were measured. The results are summarized in Table 3.

Table 3 shows D10, D50 and D90 from the F, M and B of the build bed and shows the increase in D10, D50 and D90 size from the Front to the Back of the build bed. This increase in specifically D10 and D90 shows that the volume fraction of the smaller particles decreases as from the Front to the Back of the build bed due to the recoater effect. This is inline with the proposed hypothesis and simulated studies in the literature [32]–[34] that the change in powder-bed compaction density across the build bed is due to the effect of recoater and initial powder size distribution.

Table 3: Particle size results

	D10 (μm)	D50 (μm)	D90 (μm)
F	15	28	45
M	18	32	46
B	19	34	49

3.2 Effect of relative powder-bed compaction density on AM-made parts

The results from the previous sections highlight the difference in the relative powder-bed compaction densities across the powder-bed. It is necessary to measure and quantify the effects of such differences on printed parts. If the printed parts do not show any differences from the Front to Back of the build bed, then the effect of accounting for differences in the compaction densities can be assumed to be negligible.

Using the process parameters described in Section 2.0, 12 parts (35x15x6.5 cm) were manufactured in F, M and B sections of the build bed in a configuration shown in Figure 7a. A representative sample part is shown in Figure 7b. All parts were manufactured with the same process parameters, without any support structures. The corresponding values for the density and roughness measurements are shown in Figure 9a and 9b, respectively.

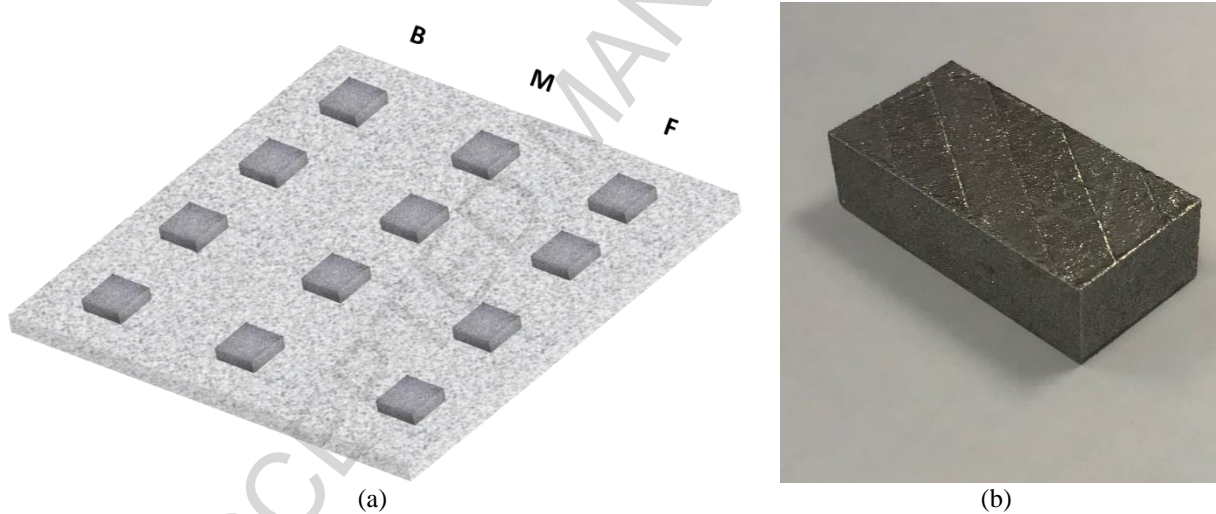


Figure 7: (a) Schematic of LPBF-made parts used to measure the effect of powder-bed compaction density on the Front (F), Middle (M) and Back (B) of build bed (b) Actual printed part

Figure 9a show the mean and error bars from F to B sections of the build bed. Results show that the density decreases slightly from the Front (99.86%) to the Back (99.79%) of the build bed with the maximum difference of $\sim 0.25\%$. The difference in the part densities can be attributed to the difference in powder-bed compaction densities and powder distribution across the powder-bed. It should be noted that density results from the LPBF parts in the literature also show a density of around 99.5% for as-built parts [35], [36].

Surface height maps from parts printed on the Front and Back of the build bed are depicted in Figure 8a and 8b, respectively. It should be noted that both maps have been normalized to have the same scale as shown in Figure 8. Other than the physical values, it can be clearly seen that the Back of the build bed exhibits relatively higher peaks (90 μm) compared to the Front (50 μm).

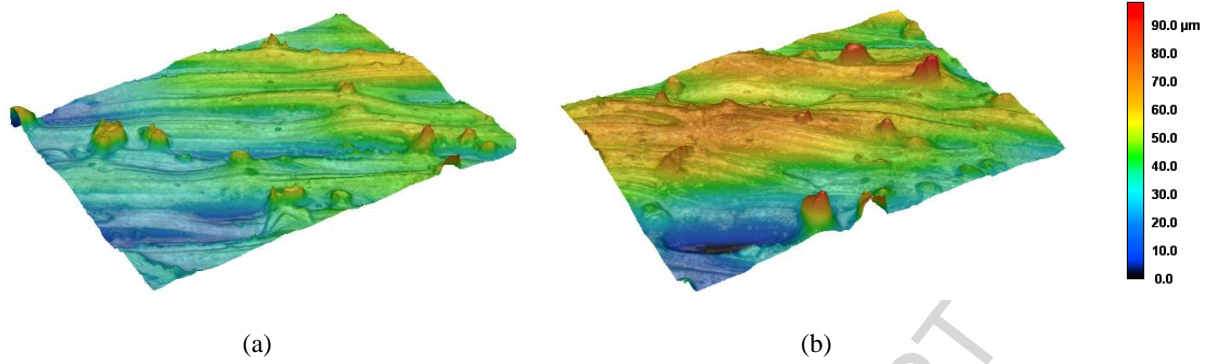


Figure 8: Surface roughness maps from the (a) Front and (b) Back of printed SLM parts

There are several ways to represent surface roughness [37]. In this work, arithmetic average of absolute values (S_a) is used to calculate the surface roughness of SLM parts and is calculated as:

$$S_a = \frac{1}{A} \iint_A z(x, y) dx dy \quad \text{Eq. 3}$$

where A is the number of points and $z(x, y)$ defines the height of each point on the surface. Figure 9b shows the mean S_a for the parts printed on the different areas of the build bed. Results show that the minimum roughness is observed on the parts manufactured at the Front (7.2 μm) followed by the Middle (7.6 μm) and Back (8.6 μm). It is noted that a surface quality improvement of almost 20% is observed between the Front and Back of the build bed. Similar to the density results, the difference in surface roughness of printed parts are attributed to the difference in the relative powder-bed compaction densities that is resulted from variable powder size distributions across the build bed.

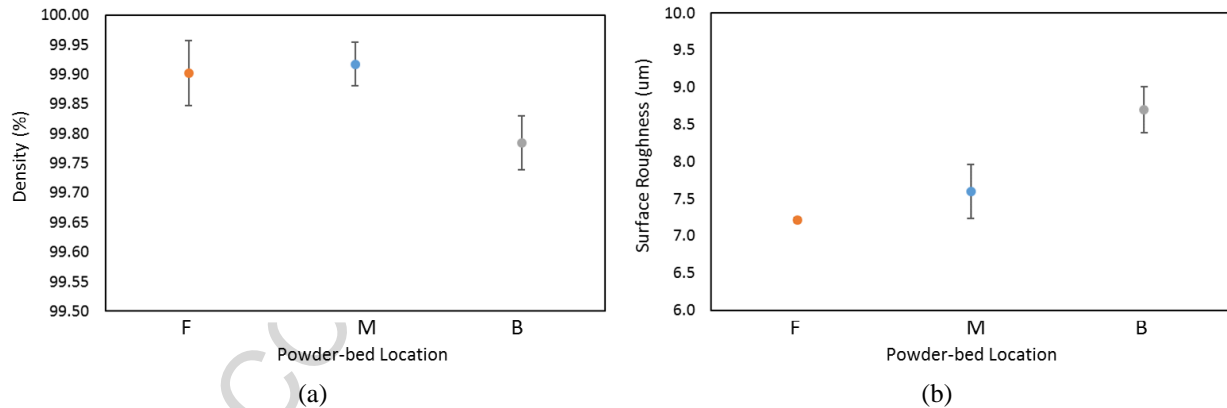


Figure 9: Experimental (a) Density and (b) Surface roughness plots on the Front (F), Middle (M) and Back (B) of the build bed

The LPBF-made parts exhibit a minor decrease in density ($\sim 0.25\%$) but a major increase in surface roughness ($\sim 20\%$) between the Front and Back of the build bed. These differences are due to the different powder-bed compaction densities and particle distribution across the build bed.

It is important to mention that the methodology to measure powder-bed compaction densities presented in this paper can be implemented to any powder-bed AM process such as binder-jet. As presented in this paper, these measurements are very important to effectively manufacture powder-bed parts. In addition, this data is very important to accurately simulate powder-bed processes as the powder-bed compaction density directly affects the powder conductivity, temperature in the melt pool and other powder properties during powder-bed AM process simulations.

Conclusions

In this work, a new methodology for the measurement of the relative powder-bed compaction density was presented. The proposed method used a UV curable polymer delivered via a precision pneumatic dispensing system to encapsulate particles and capture such samples from select locations across the powder-bed. The cured samples were then CT scanned, and the 3D images processed to obtain the relative value of powder-bed compaction densities across the build bed. The important conclusions from the conducted study are as follows:

- In line with the recoater moving direction, the powder-bed compaction density measurement results show a decrease in the compaction densities from the Front (66%) to the Back (52 %) of the build bed with a high statistical significance (p-value of 0.0052).
- The decrease in the powder-bed compaction densities across the build bed are attributed to the difference in the powder size distributions across the build compartment powder-bed from the Front to the Back of build bed. D10 - D50 - D90 values change from 15 μm - 28 μm - 45 μm to 19 μm - 34 μm - 49 μm from the Front to the Back of the build bed respectively.
- The effect of powder-bed compaction densities on the LPBF-made parts show a decrease in density (0.25%) and surface quality (20%) of the 3D printed parts from the Front to the Back of the build bed. However, compared to the density, there is a higher variation in surface roughness from the Front to the Back of the build bed. In addition, parts printed in the Back of the build bed exhibit higher surface roughness peaks (90 μm) compared to the parts printed in the Front (50 μm).

Acknowledgements

This work was supported by funding from the Natural Sciences and Engineering Research Council of Canada (NSERC) and the Federal Economic Development Agency for Southern Ontario (FedDev Ontario) and the help from Jerry Ratthapakdee and Karl Rautenberg for helping with design and print of the LPBF parts.

Data Availability

The raw data required to reproduce these findings are available to download from <https://MMESynologyMSAM.quickconnect.to/d/f/414193498286203731> . The processed data required to reproduce these findings are available to download from the same website.

References

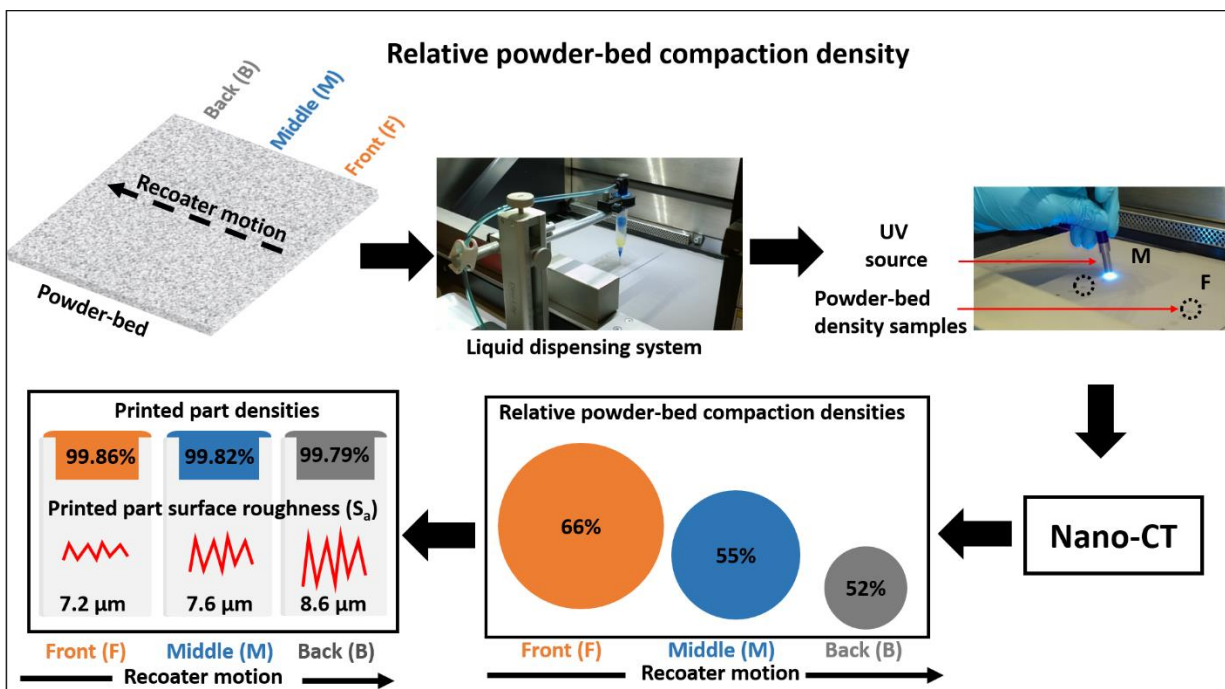
- [1] E. Herderick, "Additive manufacturing of metals: A review," *Mater. Sci. Technol. Conf. Exhib. 2011, MS T'11*, vol. 2, no. 176252, pp. 1413–1425, 2011.
- [2] D. Herzog, V. Seyda, E. Wycisk, and C. Emmelmann, "Additive manufacturing of metals," *Acta Mater.*, vol. 117, pp. 371–392, 2016.
- [3] J. Schmelzle, E. V. Kline, C. J. Dickman, E. W. Reutzel, G. Jones, and T. W. Simpson, "(Re)Designing for Part Consolidation: Understanding the Challenges of Metal Additive Manufacturing," *J. Mech. Des.*, vol. 137, no. 11, p. 111404, 2015.
- [4] Y. Hagedorn, *Laser additive manufacturing of ceramic components: Materials, processes, and mechanisms*. Elsevier Ltd, 2016.
- [5] A. M. Elliott, P. Nandwana, D. Siddel, and B. G. Compton, "A Method for Measuring Powder Bed

- Density in Binder Jet Additive Manufacturing Process and the Powder Feedstock Characteristics Influencing the Powder Bed Density,” *Solid Free. Fabr.* 2016, pp. 1031–1037, 2016.
- [6] C. Y. Yap *et al.*, “Review of selective laser melting: Materials and applications,” *Appl. Phys. Rev.*, vol. 2, no. 4, 2015.
- [7] W. E. Frazier, “Metal additive manufacturing: A review,” *Journal of Materials Engineering and Performance*, vol. 23, no. 6. pp. 1917–1928, 2014.
- [8] ASTM, “ASTM 52900:2015 Standard Terminology for Additive Manufacturing – General Principles – Terminology,” *ASTM Int.*, pp. 1–9, 2015.
- [9] K. H. Low and K. F. Leong, “Review of Selective Laser Melting process parameters for Commercially Pure Titanium and Ti6Al4V,” *Proc. 6th Int. Conf. Adv. Res. Virtual Rapid Prototyp.*, pp. 71–76, 2014.
- [10] B. Song, S. Dong, H. Liao, and C. Coddet, “Process parameter selection for selective laser melting of Ti6Al4V based on temperature distribution simulation and experimental sintering,” *Int. J. Adv. Manuf. Technol.*, vol. 61, no. 9–12, pp. 967–974, 2012.
- [11] D. Q. Zhang, Z. H. Liu, and C. K. Chua, “Investigation on forming process of copper alloys via Selective Laser Melting,” *High Value Manuf. Adv. Res. Virtual Rapid Prototyp. Proc. 6th Int. Conf. Adv. Res. Virtual Rapid Prototyping, Leir. Port. 1-5 October, 2013*, p. 285, 2013.
- [12] Y. Bai, Y. Yang, Z. Xiao, M. Zhang, and D. Wang, “Process optimization and mechanical property evolution of AlSiMg0.75 by selective laser melting,” *Mater. Des.*, 2017.
- [13] G. Jacob, A. Donmez, J. Slotwinski, and S. Moylan, “Measurement of powder bed density in powder bed fusion additive manufacturing processes,” *Meas. Sci. Technol.*, vol. 27, no. 11, 2016.
- [14] B. Liu, R. Wildman, C. Tuck, I. Ashcroft, and R. Hague, “Investigation the Effect of Particle Size Distribution on Processing Parameters Optimisation in Selective Laser Melting Process,” *Addit. Manuf. Res. Group, Loughbrough Univ.*, pp. 227–238, 2011.
- [15] T. G. Spears and S. A. Gold, “In-process sensing in selective laser melting (SLM) additive manufacturing,” *Integr. Mater. Manuf. Innov.*, 2016.
- [16] A. Hussein, L. Hao, C. Yan, and R. Everson, “Finite element simulation of the temperature and stress fields in single layers built without-support in selective laser melting,” *Mater. Des.*, vol. 52, pp. 638–647, 2013.
- [17] I. A. Roberts, C. J. Wang, R. Esterlein, M. Stanford, and D. J. Mynors, “A three-dimensional finite element analysis of the temperature field during laser melting of metal powders in additive layer manufacturing,” *Int. J. Mach. Tools Manuf.*, vol. 49, no. 12–13, pp. 916–923, 2009.
- [18] R. Andreotta, L. Ladani, and W. Brindley, “Finite element simulation of laser additive melting and solidification of Inconel 718 with experimentally tested thermal properties,” *Finite Elem. Anal. Des.*, vol. 135, pp. 36–43, 2017.
- [19] E. R. Denlinger, V. Jagdale, G. V. Srinivasan, T. El-Wardany, and P. Michaleris, “Thermal modeling of Inconel 718 processed with powder bed fusion and experimental validation using in situ measurements,” *Addit. Manuf.*, vol. 11, pp. 7–15, 2016.
- [20] Y. C. Wu *et al.*, “Numerical modeling of melt-pool behavior in selective laser melting with random powder distribution and experimental validation,” *J. Mater. Process. Technol.*, vol. 254, pp. 72–78, 2018.

- [21] S. S. Sih and J. W. Barlow, "The prediction of the emissivity and thermal conductivity of powder beds," *Part. Sci. Technol.*, vol. 22, no. 4, pp. 427–440, 2004.
- [22] N. P. Karapatis, G. Egger, P. E. Gyax, and R. Glardon, "Optimization of powder layer density in selective laser sintering," *10th Solid Free. Fabr. Symp.*, pp. 255–263, 1999.
- [23] R. K. McGEARY, "Mechanical Packing of Spherical Particles," *J. Am. Ceram. Soc.*, vol. 44, no. 10, pp. 513–522, 1961.
- [24] A. B. Spierings, N. Herres, and G. Levy, "Influence of the particle size distribution on surface quality and mechanical properties in AM steel parts," *Rapid Prototyp. J.*, vol. 17, no. 3, pp. 195–202, 2011.
- [25] H. M. Lee, C. Y. Huang, and C. J. Wang, "Forming and sintering behaviors of commercial α -Al₂O₃ powders with different particle size distribution and agglomeration," *J. Mater. Process. Technol.*, vol. 209, no. 2, pp. 714–722, 2009.
- [26] K. Darcovich, F. Toll, P. Hontanx, V. Roux, and K. Shinagawa, "An experimental and numerical study of particle size distribution effects on the sintering of porous ceramics," *Mater. Sci. Eng. A*, vol. 348, no. 1–2, pp. 76–83, 2003.
- [27] ASTM B311 - 17, "Standard Test Method for Density of Powder Metallurgy (PM) Materials Containing Less Than Two Percent Porosity," *ASTM Int. West Conshohocken*, vol. 93, no. Reapproved, pp. 1–5, 2008.
- [28] E. Sheydaeian, K. Sarikhani, P. Chen, and E. Toyserkani, "Material process development for the fabrication of heterogeneous titanium structures with selective pore morphology by a hybrid additive manufacturing process," *Mater. Des.*, vol. 135, pp. 142–150, 2017.
- [29] B. Markicevic, T. G. D'Onofrio, and H. K. Navaz, "On spread extent of sessile droplet into porous medium: Numerical solution and comparisons with experiments," *Phys. Fluids*, vol. 22, no. 1, pp. 1–12, 2010.
- [30] R. K. Holman, M. J. Cima, S. A. Uhland, and E. Sachs, "Spreading and infiltration of inkjet-printed polymer solution droplets on a porous substrate," *J. Colloid Interface Sci.*, vol. 249, no. 2, pp. 432–440, 2002.
- [31] A. Marmur, "Kinetics of penetration into uniform porous media: Testing the equivalent-capillary concept," *Langmuir*, 2003.
- [32] H. W. Mindt, M. Megahed, N. P. Lavery, M. A. Holmes, and S. G. R. Brown, "Powder Bed Layer Characteristics: The Overseen First-Order Process Input," *Metall. Mater. Trans. A Phys. Metall. Mater. Sci.*, vol. 47, no. 8, pp. 3811–3822, 2016.
- [33] H. W. Mindt, O. Desmaison, M. Megahed, A. Peralta, and J. Neumann, "Modeling of Powder Bed Manufacturing Defects," *J. Mater. Eng. Perform.*, vol. 27, no. 1, pp. 32–43, 2018.
- [34] J. Zielinski, S. Vervoort, H.-W. Mindt, and M. Megahed, "Influence of Powder Bed Characteristics on Material Quality in Additive Manufacturing," *BHM Berg- und Hüttenmännische Monatshefte*, vol. 162, no. 5, pp. 192–198, 2017.
- [35] F. Wang, X. H. Wu, and D. Clark, "On direct laser deposited Hastelloy X: dimension, surface finish, microstructure and mechanical properties," *Mater. Sci. Technol.*, vol. 27, no. 1, pp. 344–356, 2011.
- [36] D. Tomus, Y. Tian, P. A. Rometsch, M. Heilmaier, and X. Wu, "Influence of post heat treatments on anisotropy of mechanical behaviour and microstructure of Hastelloy-X parts produced by selective laser melting," *Mater. Sci. Eng. A*, vol. 667, pp. 42–53, 2016.

- [37] W. Muhammad, U. Ali, A. P. Brahme, J. Kang, R. K. Mishra, and K. Inal, "Experimental analyses and numerical modeling of texture evolution and the development of surface roughness during bending of an extruded aluminum alloy using a multiscale modeling framework," *Int. J. Plast.*, 2017.

ACCEPTED MANUSCRIPT



Graphical abstract

Highlights

- A process-independent relative powder-bed compaction density measurement technique is presented and applied to laser powder-bed fusion.
- Ultraviolet curable polymer is used to bind powder particles, followed by nano-computing tomography scanning on the bonded particles.
- Results show variation in the relative powder-bed compaction density across the build bed with meaningful effects on additively manufactured parts.